

# Raman and mid-infrared spectroscopic imaging: applications and advancements

Rekha Gautam<sup>1</sup>, Ashok Samuel<sup>1</sup>, Sanchita Sil<sup>1,2</sup>, Deepika Chaturvedi<sup>1</sup>, Abhaya Dutta<sup>3</sup>, Freek Ariese<sup>4</sup> and Siva Umaphy<sup>1,5,\*</sup>

<sup>1</sup>Department of Inorganic and Physical Chemistry, Indian Institute of Science, Bengaluru 560 012, India

<sup>2</sup>High Energy Materials Research Laboratory, Sutarwadi, Pune 411 021, India

<sup>3</sup>Molecular Biophysics Unit, Indian Institute of Science, Bengaluru 560 012, India

<sup>4</sup>LaserLaB, Faculty of Sciences, VU University Amsterdam, 1081 HV Amsterdam, The Netherlands

<sup>5</sup>Department of Instrumentation and Applied Physics, Indian Institute of Science, Bengaluru 560 012, India

**Using Raman and Mid-Infrared (MIR) spectroscopic imaging techniques one can examine the spatial distribution of various molecular constituents in a heterogeneous sample at a microscopic scale. Raman and MIR spectroscopy techniques provide bond-specific vibrational frequencies to characterize molecular species without external labelling. In addition, these techniques are rapid, non-invasive and provide multiplex advantage. In this review we discuss the instrumentation, applications and latest advancements of Raman and MIR spectroscopic imaging in various fields, ranging from materials science to medicine and illustrate with specific examples from our recent research.**

**Keywords:** Cluster analysis, explosives, FTIR imaging, polymers, Raman imaging.

MOLECULAR imaging provides a deeper insight into the composition of species under investigation, via visual representation. It provides spatially resolved chemical information that has several applications, ranging from materials science to biology. Molecular imaging enables the visualization, characterization and quantification of chemical processes in a variety of substrates including thin-films, multicomponent blends, complex biological systems and importantly living cells at cellular and sub-cellular level. Positron emission tomography (PET), single photon emission computed tomography (SPECT), magnetic resonance imaging (MRI), fluorescence imaging, computed tomography (CT), etc. are some of the well-known modalities used for basic and applied biomedical research<sup>1,2</sup> (Figure 1). In general, all imaging methods used to date have their own advantages and disadvantages and none of these can meet all the requirements of high sensitivity, noninvasive, high spatial and temporal resolution and high multiplexing capabilities. In the case of PET, SPECT, CT, etc. high energy radiations are being used and most of them require labelling that may either lead to side effects or may cause undesirable

changes at the target sites. Radionuclide imaging can probe in real-time and provides quantitative information but the image resolution is inadequate. In the area of biomedical research, fluorescence imaging with high spatial resolution is considered to be an invaluable tool to study the details of biological functions at the cellular and subcellular level. However, as only few molecules are natively fluorescent, this technique usually needs external labelling of the species and is limited by the choice of non-cytotoxic dyes, rapid photobleaching of fluorophores and the difficulty to probe multiple targets simultaneously. In contrast, label-free techniques do not require any external agent and provide informative spectral images of unmanipulated matter. Raman and MIR imaging are such label-free, non-invasive and multiplexing modalities. They can provide molecular structure and conformation-dependent spectral fingerprints of the components of heterogeneous systems with high spatial and/or temporal resolution. In the spectral imaging methodologies, spectra are often collected in mapping mode, that is, sequentially from multiple points (pixels) of the selected sample region, where the points are separated by a distance corresponding to the diffraction limit of the wavelength of the light used. This collection of spectral data is called hyperspectral data. A 2D plot of a characteristic spectral signature (e.g. intensity, position, bandwidth of a spectral band) present in the hyperspectral data is called a spectral image. Thus changes in the chemical composition at different points in space become apparent in the spectral images. In the past few decades, these techniques have been developed as important tools to probe heterogeneous samples at the microscopic level<sup>3-5</sup>.

## Raman and mid-infrared microspectroscopy

Vibrational spectroscopic techniques, Raman and MIR, probe the molecular vibrations that are specific to molecules and provide a deeper insight into the molecular composition of the sample under study. Raman spectroscopy is based on the principle of inelastic scattering of light by the molecule. The photons that give energy to the

\*For correspondence. (e-mail: umaphy@ipc.iisc.ernet.in)

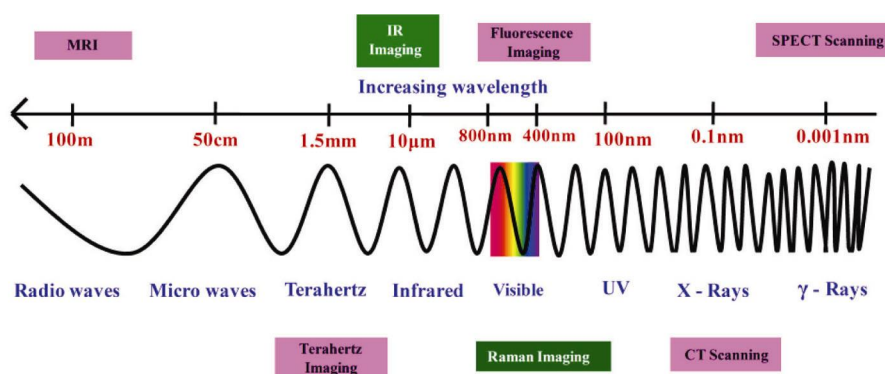


**Figure 1.** Typical wavelengths of various imaging modalities within the electromagnetic spectrum.

vibrations of the molecule generate Stokes signals, whereas photons that take up energy from an already vibrationally excited molecule give rise to anti-Stokes signals. Unlike Raman spectroscopy, infrared (IR) spectroscopy is an absorption process. In MIR spectroscopy, the radiation frequency that matches the energy difference between two vibrational levels of a molecule in a given electronic state (usually the ground state), is absorbed by the molecule and leads to vibrational transitions. Almost all molecular vibrational modes absorb light in the MIR range (2.5–25  $\mu\text{m}$ ). Raman and IR transitions are complementary to each other. The molecular vibrations that lead to a change in the dipole moment are IR active whereas the vibrations that lead to a change in polarizability of the molecule are Raman active. According to the principle of mutual exclusion, for a molecule with inversion symmetry, vibrations that are Raman active are IR inactive and vice-versa. For a complex molecule with no symmetry (except identity element) all the normal modes are both Raman and IR active. The integration of a spectrometer with an optical microscope led to the detection of spectra from microscopic sample regions that are not visible to human eye. Further, this modification allows addressing chemical heterogeneity of a sample at micrometer and submicrometer levels. Raman and IR microspectroscopic techniques have witnessed a rapid advancement in the last two decades<sup>5</sup>. A more detailed description of Raman and MIR microspectroscopy is given in the following sections.

### Raman microspectroscopy

Since the Raman scattering is intrinsically weak, Raman researchers of the late 1950s were of differing opinion regarding the collection of Raman spectra from micron-sized samples. Some argued that signals from such small numbers of molecules would be too weak to extract substantial information. However, Delhaye and Migeon<sup>6</sup> explained that the intensity of the Raman signal remains constant with the decrease in laser spot size up to the

diffraction limit. They reasoned that the decrease in the Raman signals due to the small quantity of the sample would be compensated by the advantage of tight laser focus and high collection efficiency provided by high numerical aperture objective lenses. Within a few years (1974), Raman microscopes were built simultaneously in two locations, one by Dhamelincourt and another by a student of Delhaye<sup>6,7</sup>. Since then, the advent of more user-friendly lasers, highly efficient holographic notch filters, gratings and multichannel detectors revolutionized the field of Raman microspectroscopy.

The integration with a microscope provided an easy visualization of micron-sized objects and allowed the detection of their Raman spectra. In addition, this provided the flexibility to choose the area of interest within a heterogeneous sample with a high magnification objective lens. Usually a Raman microscope works at 180° geometry, i.e. the excitation as well as the collection of Raman signals from the sample is performed with the same objective lens. The numerical aperture (NA) of the objective lens determines the spatial resolution and collection efficiency of a microscope. In a simplified form, the diffraction limited lateral resolution ( $R$ ) can be approximated as the spot size of the laser focus and could be estimated as:  $R \sim \lambda/2\text{NA}$ , where NA, the numerical aperture of the objective =  $\eta \cdot \sin\theta$ ,  $\eta$  is the refractive index of the medium,  $\theta$ , half of the maximum cone angle of light that can enter or exit the lens, and  $\lambda$  is the excitation wavelength. For a better spatial resolution  $R$  should be smaller and thus an increase in NA improves the spatial resolution. Higher NA can be achieved either by increasing  $\theta$  or by increasing the refractive index of the medium between the objective lens and the sample. In the case of dry objectives the maximum possible value of NA cannot exceed 1 as the refractive index of air ( $n_{\text{air}}$ ) is 1 and  $\theta$  cannot practically be increased beyond 72°. However, the spatial resolution can be improved further by increasing the refractive index of the medium by using water ( $n_{\text{water}} = 1.3$ ) or oil ( $n_{\text{oil}} = 1.5$ ) immersion objectives. Spatial resolution has two aspects: the lateral resolution ( $x$  and  $y$  direction) in the plane perpendicular to the

optical axis and the axial or depth resolution (along the optic axis). In order to further improve the depth resolution ( $z$  direction), a confocal configuration with a pinhole is generally employed. In this arrangement a pinhole is placed at the conjugate focal plane in the scattering collection path. The confocal setup efficiently prevents out-of-focus light and unwanted signals from entering the detector. The confocal arrangement limits the detection volume, which helps improve the signal-to-background ratio (e.g. reducing the fluorescence background). Thus the resulting Raman images from thin sections of the sample also have much better contrast and enable us to construct the three-dimensional images of the sample by optically sectioning (slicing) the sample<sup>8–11</sup>. Three major conventional methodologies generally employed to obtain Raman spectral images are described below in detail.

**Point, line and wide-field imaging modes:** The principal aim of Raman imaging is to get separate spectral images of molecular species present in the sample on the basis of their spectral differences. Raman imaging is frequently acquired by using (i) a spot focus, (ii) a line focus, or (iii) global (wide-field) illumination and confer three-dimensional, two spatial and one spectral, information<sup>12,13</sup>.

In the case of point scanning (mapping), the spatial region of interest is scanned with a single point focus to generate a two-dimension (2D) image. After collecting spectrum from one point in the sample, the focus point is moved to the next point, separated by a predetermined step-size. When the step size is larger than the diffraction limited spot size ( $R$ ) the specimen is said to be under-sampled and if the step-size is smaller than  $R$ , it is said to be over-sampled. By repeating the process in both  $x$  and  $y$  direction one acquires a hyperspectral data set (Figure 2 *a*). This point mapping technique maintains the spatial resolution and the laser power as provided by the objective, i.e. near to the diffraction limit<sup>14</sup>.

In the case of a line scanning mode the sample is scanned with a line focus. Two different methods are currently used to create a line focus: (i) the conversion of a circular beam to a line focus using a cylindrical lens (ii) the point focus is rapidly moved to construct a line (Figure 2 *b*). In the former case the line is produced at the focal plane of the microscope by placing a cylindrical lens in the excitation beam and is aligned vertically to produce an image elongated along the slit axis. The focal length and diameter of the cylindrical lens determines the dimension of the line-focus, which usually is far away from the diffraction limit<sup>15</sup>. Moreover, the laser intensity varies along the line focus in case of a cylindrical lens focus and gives rise to artifacts in the Raman image generated. As an advantage, the laser power density at the sample is decreased by a large factor and hence the probability of photo damage is reduced. In the second case, the point focus is scanned to construct a line by using

synchronized movable mirrors, thus maintaining a uniform illumination<sup>13</sup>. In line-focus illumination, the diffraction limited spatial resolution is achievable in the direction perpendicular to the laser line-focus, whereas in the other dimension (along the line focus) the spatial resolution is determined by the convolution of the microscope magnification at the detector and the CCD pixel size. The laser line is oriented parallel to the entrance-slit of the spectrometer and scattered light is collected by a row of pixels of the CCD from a discrete position along the slit axis. For example, a  $256 \times 1024$  CCD collects 256 spatial positions along the line focus and 1024 spectral features (Raman shift values) in a single integration. In order to generate an image, the sample is then mechanically scanned with the line-focus. Since the line-focus in the present case is equivalent to a 1D array of single foci, the technique is faster than the single focus mapping methodology. Furthermore, a confocal arrangement can be implemented with both point and line scanning modes but a faster image acquisition is an advantage of the line-focus illumination.

Global imaging or wide-field imaging is the technique where a large area of the sample is illuminated and the 2D image is constructed in a single measurement at a particular wavenumber. In this case two dimensions of the CCD are used to acquire spatial information and the spectral region of interest is selected using tunable, narrow band-pass filters (Figure 2 *c*). Alternatively, one can also tune the laser wavelength relative to a fixed filter wavelength to probe a certain Raman frequency<sup>16</sup>. Generally global illumination is achieved by defocusing the laser and consequently the power density is much lower than the tight point focus. Also, wide-field illumination probes a larger area of the sample within the field-of-view of the microscope at the expense of spectral information and it provides poorer spatial resolution in both dimensions. In

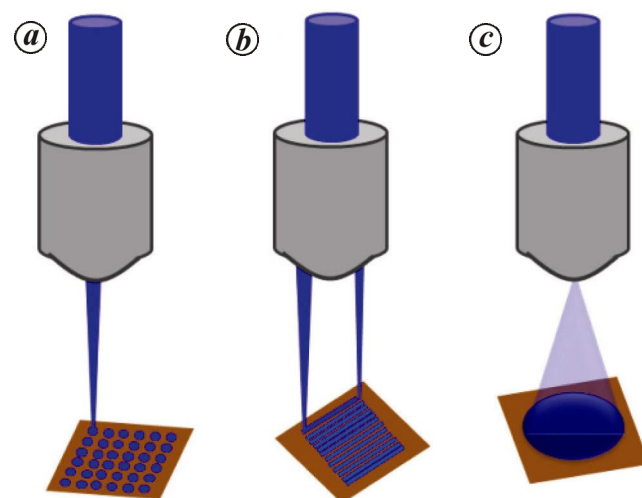


**Figure 2.** Schematics of imaging methodologies: *a*, Point scanning; *b*, Line scanning; *c*, Wide-field or global imaging.

addition, global imaging suffers from poor depth resolution since there is no confocal arrangement (pinhole)<sup>16–18</sup>. On the other hand, wide-field imaging has the advantage of rapid image acquisition and is therefore suitable for probing the dynamics. This is because a large area of the sample is probed simultaneously. The choice of the imaging technique is often critical and depends on the type of experiment. If the spectral information of the molecular constituents in the sample is known prior to imaging, one could prefer global imaging to the scanning methodologies. On the other hand, if the spectral constituents and its spatial distribution are unknown, then point or line scanning methodologies that provide complete spectral information can be used in conjunction with the multivariate analysis. All three imaging methodologies are being widely used and some of those applications are discussed later in this review.

*FTIR microspectroscopy:* In 1800 William Herschel, an English astronomer, discovered IR radiation as a discrete region of the electromagnetic spectrum. However, the field of IR spectroscopy remained under-explored for many decades after this discovery due to expensive optical elements and unavailability of suitable detectors to measure IR radiation. In 1882, Abney and Festing captured pictures of absorption spectra of about fifty compounds and recognized that absorption bands are characteristic of certain organic functional groups. Later, Coblentz measured the spectra of hundreds of inorganic and organic substances, which were published in 1905 and this work laid the foundation for analytical IR absorption spectroscopy by identifying specific organic functional groups. In 1930 the first IR spectrometer was constructed, which led to the rapid development in the field of analytical IR spectroscopy. These earlier instruments used dispersive spectrometers based on prism or grating monochromators. After the World War II the advancement in electronics brought the thermocouple detector technology that led to the next breakthrough in IR spectroscopy. In 1947, Wright and Hersher developed a stable double beam dispersive spectrophotometer and thereafter IR spectroscopy was recognized as an analytical tool, both in academic and industrial labs. In 1949, Barer, Cole and Thompson coupled microscopy and IR spectroscopy, in which they used a dispersive IR spectrometer. Later the discovery of Fourier transform infrared (FTIR) spectrometers revolutionized the field of IR spectroscopy. This new development utilized a Michelson interferometer (invented by Albert Abraham Michelson) and a mathematical procedure developed by Joseph Fourier, called the Fourier transformation, to convert an interferogram into a spectrum. There were several computational complexities associated with the Fourier procedure, but in 1949 Fellgett provided a solution to solve this problem. He also realized the multiplex advantage of FT spectroscopy (i.e. all wavenumbers of the light are

observed simultaneously), which is called the ‘Fellgett advantage’. After a few years, in 1954, a French scientist, Jacquinot explained the throughput advantage of interferometry (FTIR) instrument over dispersive ones, as FTIR spectrometers do not require slits. The practical implication of these advantages improved the acceptance of FTIR spectroscopy. More recently, FTIR spectroscopy witnessed a significant growth with the advent of fast Fourier transform algorithms and dedicated computers. Digilab launched the first commercial FTIR microspectrometer with Spectra-Tech in 1983. Since then, FTIR microspectroscopy has been widely used as an analytical tool in various fields of research<sup>19,20</sup>.

Similar to Raman microspectroscopy, IR microspectroscopy also combines the benefits of both high spatial resolution and rich chemical information of the sample composition. Since glass optics absorb wavelengths longer than 4.5  $\mu\text{m}$ , they are not suitable for MIR (2.5  $\mu\text{m}$  to 25  $\mu\text{m}$ ) microscopy. Therefore, the MIR microspectroscope uses all-reflecting optics with aspherical reflecting surfaces in a Cassegrain-type configuration for minimizing optical aberrations. The transmittance, reflectance and trans-reflectance approaches are the most popular sampling approaches because of the ease of sample preparation and experimental design. Due to the long wavelength of MIR radiation the spatial resolution of IR-based microspectroscopes is poorer compared to Raman microspectroscopes that use light of shorter wavelength (UV-visible range). The typical value of NA in MIR microscope objective lenses ranges from 0.3 to 0.7 with different choice of magnifications such as 6 $\times$ , 15 $\times$  and 32 $\times$ . Owing to the development of more stable, sensitive, fast-response cryogenic detectors, motorized stages and digital spectral processing it is now possible to obtain spectral images with IR microspectroscopy. Two main approaches are in practice, one is mapping and another is imaging (Figure 3). FTIR mapping employs a single-element detector, an aperture and a motorized high precision stage, which allows a point-by-point examination of the sample region (it is equivalent to single-point scanning methodology used in Raman microspectral imaging). However, this methodology has the following limitations: (i) at high spatial resolution (aperture dimensions approach the wavelength of light) IR spectral images take several hours to maintain data quality, (ii) the single-element detector size is usually 250  $\times$  250  $\mu\text{m}$  or larger, therefore small apertures (5–50  $\mu\text{m}$ ) with 1:1 magnification between sample plane and detector lead to a poor signal to noise ratio. This is compensated either by including magnification optics between the sample plane and the detector or by incorporating a smaller detector (25–100  $\mu\text{m}$ ), but the exact matching of the size was not feasible and it is difficult to design optimal optics for different aperture sizes.

The more recent approach of imaging employs multi-channel focal plane array (FPA) detectors. An FPA is an

array of several small detection elements (pixel,  $40 \times 40 \mu\text{m}$ ) and the configurations vary from  $1 \times 16$  linear (1D) array to  $64 \times 64$  (or  $128 \times 128$  or even  $256 \times 256$ ) 2D array detectors. The implementation of FPA detectors in IR imaging methods allows a direct access to images with better spatial resolution (approaching the mid-IR diffraction limit). Since the images are acquired in single shot (all pixels simultaneously), spatially resolved molecular and structural information of the area analysed could be obtained within a few minutes<sup>20,21</sup>. Applications of the vibrational spectroscopic imaging techniques to address specific questions in materials and biology shall be briefly discussed in the following sections by citing specific examples from our own research.

### Examples of applications

In order to analyse the spatially resolved chemical information contained in the hyperspectral data, the intensity distribution of individual spectral components is plotted as an image. This information can provide the distribution of molecular species on a heterogeneous substrate. Two interesting applications of spectral imaging in polymer thin films are discussed in the following section: (a) phase separation in blends; (b) surface morphology of porous thin films. The subsequent section highlights applications of Raman and MIR imaging for the detection and

characterization of various molecules (e.g. explosives, graphene, drugs, etc.), as well as cells and tissues.

### *Phase separation and surface morphology of polymer thin films*

Phase separation in polymers has been studied over the last few decades<sup>22</sup>. Differential scanning calorimetry (DSC), small angle X-ray scattering (SAXS), polarized optical microscopy (POM) and electron microscopy have been utilized to gather information on the phase behaviour of polymeric systems. The advent of spectral imaging allows the direct retrieval of chemical information from such polymeric systems. For instance, the difference in chemical composition along the rim of pores in a porous polymeric film of a block copolymer has been demonstrated using Raman imaging techniques<sup>23</sup>. Raman imaging analysis also helped to identify impurity characteristics of phase-separated domains in a binary polyfluorene composite thin film<sup>24</sup>, which is critical for its performance in optoelectronic devices. The sensitivity of Raman spectroscopy is comparable to that of DSC in detecting chemical phase separation in binary mixtures. In addition, in some samples with barely detectable glass transitions, the Raman technique proved superior to this conventional analytical technique<sup>25</sup>. Several other interesting applications of the technique can be found in a recent review<sup>26</sup>. Here we discuss one of our recent studies on polymethylmethacrylate/polyethyleneoxide (PMMA/PEO) blends. The PMMA/PEO system is particularly interesting, since multiple kinetic events are involved in the phase separation mechanism and a true picture of temperature effects has so far remained elusive<sup>27</sup>.

A thin film of PMMA/PEO was prepared by casting a solution of a mixture of PMMA and PEO (1 : 1 weight ratio) in chloroform. PMMA and PEO remain miscible in the thin film but crystallization of PEO leads to phase separation. White light and POM images of a selected region of this film (at  $35^\circ\text{C}$ ) are shown in Figure 4 a and b. The spatial distribution of PMMA and PEO is not directly evident from these images. A Raman spectral imaging experiment was performed on the same sample region in order to study the differences in the distribution of constituents when the phase separation occurs at different isothermal conditions. The Raman band corresponding to methylene rocking vibration of the backbone appears at  $802 \text{ cm}^{-1}$  for PMMA and that for crystalline PEO appears at  $844 \text{ cm}^{-1}$  (Figure 4 i). The appearance of the PEO band at  $844 \text{ cm}^{-1}$  indicates that the polymer adopts a helical configuration in the phase-separated blend with a TGT (trans-gauche-trans) configuration about the O–C–O segments<sup>28</sup>. The  $844 \text{ cm}^{-1}$  band changes to a broad band centred at  $810 \text{ cm}^{-1}$  when PEO melts. Our studies indicated that the C–O trans conformation changes to C–O gauche conformation when the

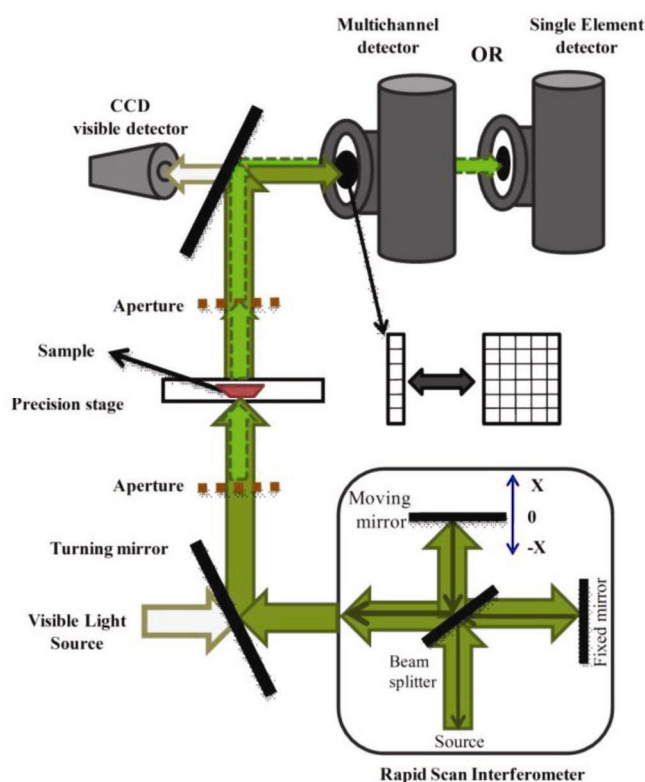


**Figure 3.** Schematic of operation of IR microscope, with single element detector and with multichannel detector.

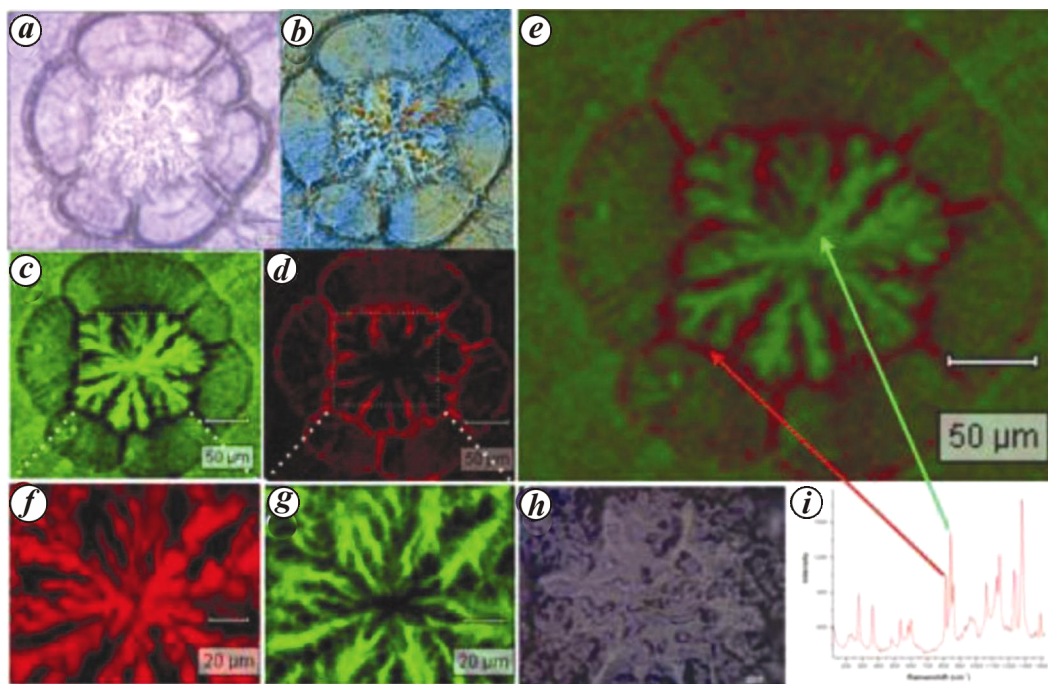


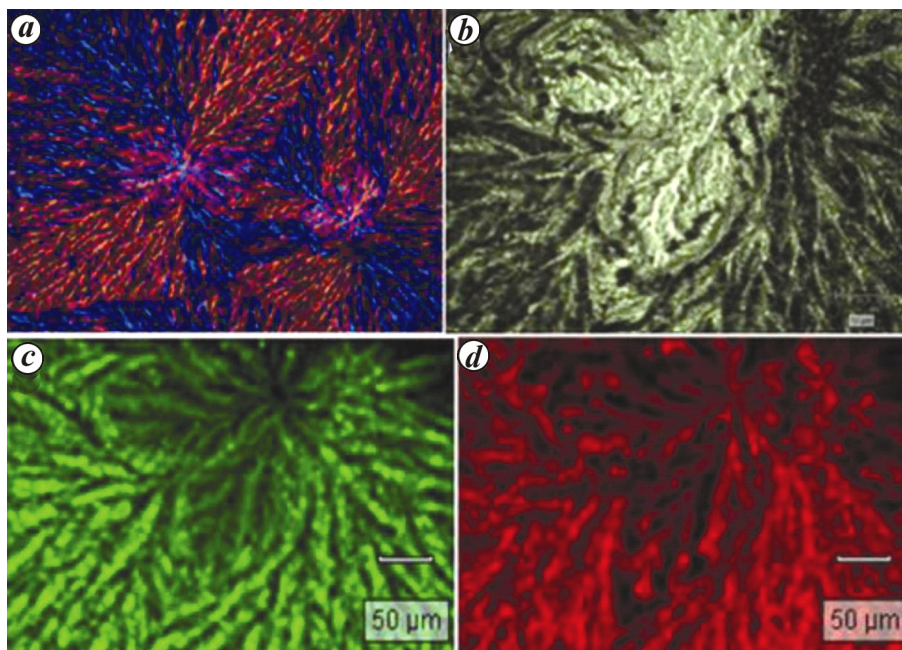
**Figure 4.** Raman imaging of PMMA/PEO thin film, prepared at 35°C. (a) white light image (b) the corresponding polarized optical microscopy image. The Raman images were obtained by plotting the intensity of the  $844\text{ cm}^{-1}$  PEO band (c) and the  $802\text{ cm}^{-1}$  PMMA band (d) and an overlay (e), recorded from the same spatial region using a  $20\times$  microscope objective. The high resolution Raman images were recorded using a higher magnification ( $50\times$ ) objective (f and g) and the corresponding spatial region under white light (h). A Raman spectrum of the PMMA/PEO blend is also provided (i).

polymer melts, while the C–C gauche conformer remains unchanged<sup>28</sup>. The intensity distribution of  $810\text{ cm}^{-1}$  and  $844\text{ cm}^{-1}$  bands (images) gives an insight into the spatial distribution of each chemical component in the blend. The Raman images (Figure 4 c, d) clearly demonstrate the phase separation between the components (unpublished work). The pixels with high intensity of the  $844\text{ cm}^{-1}$  band are represented in green colour and that of the  $802\text{ cm}^{-1}$  band in red colour (Figure 4 c, d and e). It is clear from the Raman images that the distribution of PEO is different from that of PMMA; the areas that are rich in PMMA have nearly zero contribution from PEO, suggesting a complete phase separation. An image recorded using a higher spatial resolution ( $50\times$  objective) microscope objective (see the marked regions in the corresponding images), is also provided in Figure 4 f and g. Similar features were also observed in the high-resolution image and hence the spatial resolution of the instrument is adequate to resolve features in the thin film.

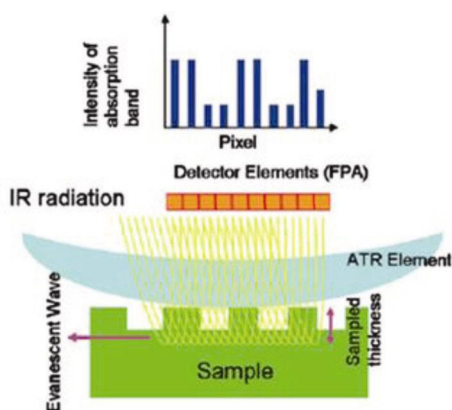
It is well known that the rate of crystallization is different at different temperatures. The rate of crystallization of PEO is one of the main factors affecting the phase separation of PMMA and PEO in the blend. Hence changes in PEO crystallization kinetics would influence the mechanism of phase separation, which in turn affects the nature of segregation of individual components of the blend in the thin film. In order to investigate the influence of temperature on the phase separation, studies were also conducted at a different temperature ( $45^\circ\text{C}$ ). An

image of the PMMA/PEO film at  $45^\circ\text{C}$  is provided in Figure 5 (unpublished work). A clear difference in the spatial distribution of PMMA and PEO is evident at  $45^\circ\text{C}$  when compared to the film at  $35^\circ\text{C}$  (Figure 4). This indicates that there is a competition between different kinetic processes during phase separation (e.g. the rate of crystallization, the rate of nucleation, etc.) that leads to differences in the distribution of chemical components in the thin film. Since  $45^\circ\text{C}$  is close to the melting point of PEO ( $65^\circ\text{C}$ ), crystal nuclei formation will be a rare occurrence. Hence the nuclei formed will slowly grow with time and the crystalline PEO domains will extend to a larger distance like a thread (Figure 5). On the other hand, at  $35^\circ\text{C}$  several nuclei form simultaneously and will grow and fuse together, leading to a bulk and isolated domains of PEO (Figure 4). A detailed study of the influence of different kinetic factors is currently in progress. However, using this specific example, we have demonstrated the utility of Raman imaging to address the spatial distribution of chemical constituents during polymer phase separation. Several pieces of unique information, such as the reason for the appearance of different morphologies in the thin film during phase separation and the dependence of the crystalline domain size on temperature, were obtained using Raman imaging and were rather difficult to obtain from other imaging techniques.

Surface morphology is another important feature of polymer thin films. Atomic force microscopy (AFM) and scanning electron microscopy (SEM) are the two widely



**Figure 5.** Raman imaging of PMMA/PEO thin film, prepared at 45°C. Polarized optical microscopy image (a) and white light image (b). The Raman images were obtained by plotting the intensity of the 844  $\text{cm}^{-1}$  PEO band (c) and the 802  $\text{cm}^{-1}$  PMMA band (d).



**Figure 6.** Schematic representation of ATR-IR, illustrating the interaction of the IR evanescent wave with the sample and the intensity profile created in the FPA detector because of the variations in the material in the effective sampling thickness (depth of penetration). Reproduced from Reference 30 with permission.

used techniques for such analyses. Optical techniques could be effectively used for studying the surface characteristics of thin films by limiting the detection volume to the required thickness (Figure 6). ATR-IR spectroscopic imaging, which works on the principle of attenuated total internal reflection (ATR), is well suited for studying such surface features. In ATR-IR spectroscopy a high refractive index material (e.g. Ge, diamond, etc.) is used as an ATR element, which is placed in front of a Cassegrainian objective lens. The IR beam undergoes total internal reflection at the outer surface of the ATR element (angle of incidence  $>$  critical angle) and generates an evanescent

wave, which travels a small distance perpendicular to the surface. The intensity of the evanescent wave decays exponentially as a function of distance from the surface. Consequently, most of the ATR-IR signal will be recorded from a thickness corresponding to the depth of penetration ( $d$ ) of this evanescent wave.  $d$  is a function of the refractive indices of the sample and the ATR element as well as the wavelength of IR, and is close to a micron at 1000  $\text{cm}^{-1}$  for the PMMA-Ge interface<sup>29</sup>. The attenuated IR beam from the field-of-view of the ATR element when observed using a single element detector gives a single spectrum. At the same time, observing the same region using a pixilated focal plane array (FPA) detector provides hyperspectral data, which could be analysed by plotting images of individual spectral components separately. The presence of any surface features (e.g. pores) within this depth would be revealed in the spectral images. A simplified pictorial representation of this process is provided in Figure 6. The evanescent IR wave samples only a thin top layer of the sample, indicated as 'sampled thickness'. An array of detector elements in a FPA detector and the intensity of a selected IR band at these pixels (corresponding to a particular spatial region) are also depicted in Figure 6. This intensity modulation reflects the structural features in the sampled region.

We have applied this technique to study the morphology of porous PMMA thin films. The thin films were prepared by the water phase separation strategy recently developed<sup>29</sup>. An ATR-IR image of the porous film is provided in Figure 7; the porous features are clearly visible in the 2D as well as 3D images. The image represents

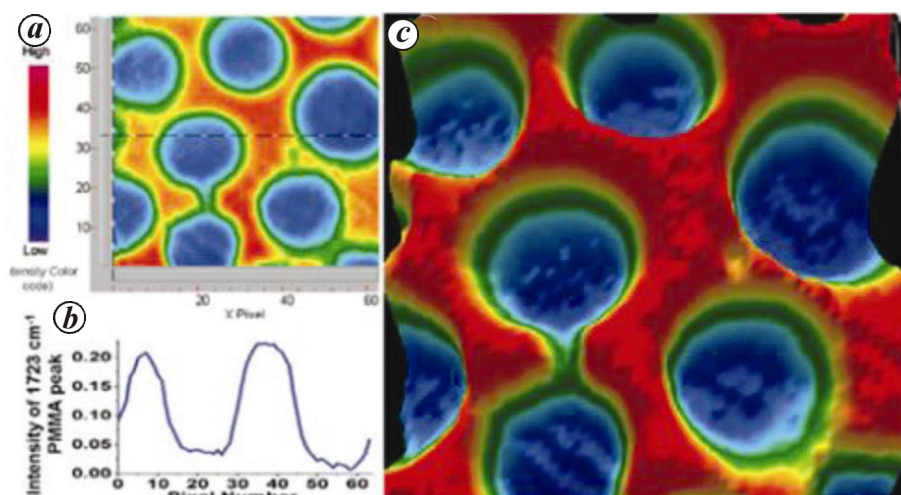


**Figure 7.** ATR-IR imaging of surface pores; intensity distribution of PMMA peak in (a) 2D and (c) 3D plot. Images recorded from porous PMMA film prepared using 90  $\mu\text{l}$  of SDS solution in water (0.82 mM). (b) Intensity variation (line profile) of the  $1723\text{ cm}^{-1}$  carbonyl peak along the dotted line (pixel position) in image (a). Scale –  $64 \times 64\ \mu\text{m}^2$ . Reproduced from reference 30 with permission.

the intensity distribution of the C=O stretching vibration of the ester carbonyls in PMMA ( $1723\text{ cm}^{-1}$ ). The PMMA peak intensity goes to zero in the region of the pores (no PMMA present). A plot of the intensity profile (variation of intensity) along the line indicated in Figure 7a is provided alongside the image in Figure 7b. The pore sizes were estimated from the line profiles. A good agreement was obtained between the pore sizes estimated from ATR-IR images and AFM images. This demonstrates the ability of spectral imaging to address the surface morphology of thin films.

#### Identification and characterization of various molecules, cells and tissues

Raman imaging techniques were also found to provide a comprehensive way to characterize carbonaceous materials such as graphene, carbon nanotubes, etc. These materials are known to quench fluorescence either via electron transfer or energy transfer and hence enhance the visibility of Raman signals from fluorescing substances<sup>30</sup>. Raman spectroscopy and imaging was used as a fast and sensitive method to characterize the graphene layers and to study the effects of substrates, the top layer deposition, the annealing process, as well as folding (stacking order) on the physical and electronic properties. It has been argued that the Raman analysis of graphene would be helpful in developing a better understanding of its physical and electronic properties<sup>31</sup>.

Detection of explosives is one of the challenges faced all around the globe. Several approaches have been adopted and the search for faster and more sensitive techniques is always ongoing. In this regard Raman spectroscopy has emerged as a potential candidate. This technique

provides not only structural information but has also been useful in the imaging field. Emmons *et al.*<sup>32</sup> have used Raman global imaging to identify explosives in contaminated fingerprints. They have used Pearson's cosine cross-correlation to determine the spatial distribution of the different explosives despite the presence of interferences such as skin fragments and skin oil<sup>32</sup>. Similarly, trace amounts of explosives were detected on human nail using Raman point mapping of PETN (pentaerythritol tetranitrate) crystals under nail varnish, acquired at the  $1290\text{ cm}^{-1}$  (symmetric ( $\text{NO}_2$ ) stretching)<sup>33</sup>. Ali *et al.*<sup>33</sup> argued that the contamination of the nail can result from the manual handling, packaging or transportation of explosive substances and hence can be used for security purposes or as a strong forensic evidence to link these hazardous substances to individuals involved in possible terrorist activities.

In the present work we demonstrate Raman imaging of 1,3,5-trinitro-1,3,5-triazacyclohexane, commonly known as RDX, in different matrices. 10  $\mu\text{l}$  of millimolar concentration of RDX in acetone was dropped on cloth and on a uniform silica-soil matrix, covering an area of  $1\text{ mm} \times 1\text{ mm}$ . Raman spectral images were acquired with a Renishaw InVia Raman microscope using a  $20\times$  objective and  $785\text{ nm}$  excitation laser with a  $1\ \mu\text{m}$  step size and an integration time of 5 sec. Raman images were colour coded with respect to the  $883\text{ cm}^{-1}$  band, a sharp Raman peak that corresponds to a ring breathing mode. These images show the distribution of RDX on the fabric matrix (Figure 8a(ii)), silica matrix (Figure 8b(ii)) and silica-soil blend matrix (Figure 8c). The top row (i) of Figure 8 shows the corresponding white light images. This study demonstrates the potential of Raman imaging in detection of explosives in real matrices.

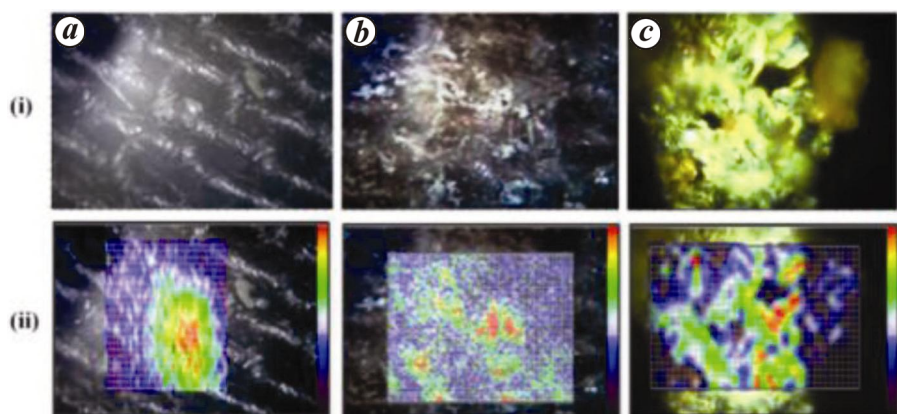


**Figure 8.** Distribution of RDX over (a) fabric matrix, (b) Silica matrix, (c) silica-sand blend matrix. Row (i) represents the white light images and row (ii) represents the corresponding Raman images, colour coded with respect to the  $885\text{ cm}^{-1}$  band.

Raman and IR microspectroscopy have also been widely used for the identification and characterization of drugs and in addition helped monitor drug delivery and drug toxicity mechanisms<sup>34–36</sup>. Widjaja *et al.*<sup>34</sup> have performed point-by-point Raman mapping measurements and band-target entropy minimization (BTEM) analysis on double walled microsphere (DWMS) samples to get the pure component spectra. Their results confer that the combination of Raman microscopy and BTEM analysis is a sensitive and specific tool to characterize DWMS. It can provide the spatial distributions of various chemical species present and therefore can serve as a complementary tool to other more established analytical techniques, such as scanning electron microscopy (SEM) and optical microscopy. They discussed that DWMS can provide better control of drug release compared to conventional single polymer microspheres, and the proposed method can be readily extended to study, the drug distribution and *in situ* drug release studies with DWMS<sup>34</sup>. Bratashov *et al.*<sup>35</sup> demonstrated that Raman characterization provides additional static and dynamic molecular information in comparison to that obtained using optical microscopy and AFM in the study of the composition, stability, and photodegradation of polyelectrolyte multilayer microcapsules and coated microparticles containing copper-phthalocyanine and iron-phthalocyanine. Transdermal drug delivery (TDD) systems have the advantages of highly controlled delivery rates, avoidance of gastrointestinal irritation and the effective usage of drugs with short biological half-lives. A commonly used TDD system employs a reservoir of the active ingredients and carriers to maintain a constant drug level. Mostly copolymers of vinyl acetate and ethylene (EVA) are applied as the rate-controlling membrane in these systems. There is a need for a single analytical method which can make modified TDD characterization and design much more efficient and vibrational imaging techniques have shown perspective for that purpose. Rafferty *et al.*<sup>36</sup> studied the diffusion of

nicotine in ethanol/water mixtures into an ethylene-vinyl acetate (EVA) copolymer membrane by FTIR imaging and the spatial and temporal distribution of each component in the EVA membrane was depicted through FTIR images. They revealed that a broad range of data, which is required to characterize a TDD system, can be obtained by this technique and that is otherwise attainable only by the use of multiple analytical techniques. Drug-induced toxicity contributes to a significant percentage of patient morbidity and mortality and is the leading cause for the un-approval and withdrawal of drugs from the pharmaceutical market<sup>37–39</sup>. Raman and IR imaging are routinely used for *in vitro* toxicological evaluation of pharmaceuticals in live human cells and model organisms. Raman micro-spectroscopy with multivariate analysis was employed to monitor the effects of an antitumour drug (gemcitabine), currently used in the treatment of lung cancer, on single living cells of a lung cancer cell line, Calu-1 (ref. 37). The cells were exposed to cytostatic doses (1 nM to 1 mM for 24 h and 48 h) and the Raman maps of single living cells were acquired to monitor the impact of an anti-tumour drug on the distribution of major macromolecules in a label-free manner. The authors suggested that from an oncological point of view, Raman spectroscopy of single cells can be useful not only for drug screening on tumour cells *in vitro*, but also for rapidly evaluating cell response to chemotherapeutics. FTIR could also be explored in toxicology to understand the metabolic responses of living systems to pathophysiological stimuli and for the characterization of new animal models for idiosyncratic susceptibility<sup>38</sup>.

Using FTIR imaging, we have also examined the effect of acetaminophen (paracetamol), an analgesic and antipyretic drug that is extensively used for therapeutic purposes<sup>39</sup>. In this study, hepatotoxicity in mice post oral dosing of acetaminophen was investigated using liver and sera samples. The IR spectra of acetaminophen-treated livers in mice show a decrease in the glycogen triad at

1030, 1080 and 1152  $\text{cm}^{-1}$  with respect to the control (Figure 9b). The FTIR false-coloured functional group images were reconstructed at 1030/1080  $\text{cm}^{-1}$  using Cytospec software. These images represent the correlation of glycogen decrease with injury in liver tissue, where the colour scale from red to blue represents the highest and lowest glycogen values respectively (Figure 9a). The recovery experiments using L-methionine demonstrated that pre L-methionine treatment ( $-0.5$  h), but not post treatment, restored glycogen (Figure 10).

Raman and IR spectroscopic methods are also being used to classify and identify biothreat organisms in the presence of complex environmental backgrounds, without the use of amplification or enhancement techniques<sup>40-42</sup>. These studies will be further applicable to detect the spatial distribution of pathogens in case of surface contamination, bioaerosols, waterborne pathogens, foodborne pathogens and in clinical samples. Usually various pathological states are identified by morphological changes which are accompanied by changes in composition and structure of assorted biomolecules such as proteins, lipids, nucleic acids, etc. they can be probed by Raman and MIR spectroscopy<sup>43,44</sup>. The biochemical composition of the

nerve membrane and structural organization of nerve fibre has been studied by different biochemical and biophysical techniques. Under steady state conditions, the conformation of membrane lipids remains stable. However, a number of toxicants and anaesthetic molecules change the membrane fluidity which can be probed using Raman spectroscopy as it is sensitive to backbone structural changes<sup>45,46</sup>.

Stem cells are pluripotent and have the ability to proliferate indefinitely and therefore have great potential in tissue engineering, drug screening and for treatments of many diseases like cancer. The main constraint is to differentiate efficiently and to produce homogeneous populations of the desired cell types. Raman and IR are also recognized as important tools for probing stem cells at the molecular level for screening and to understand their differentiation status<sup>47-49</sup>. Ami *et al.*<sup>48</sup> observed the differentiation of murine embryonic stem (ES) cells and identified marker bands of ES cell differentiation using FTIR along with multivariate analysis. Raman imaging applications to live cells are restricted as the time required for an appropriate SNR Raman images is quite high. Pascut *et al.*<sup>49</sup> have applied Raman micro-spectroscopy to the field

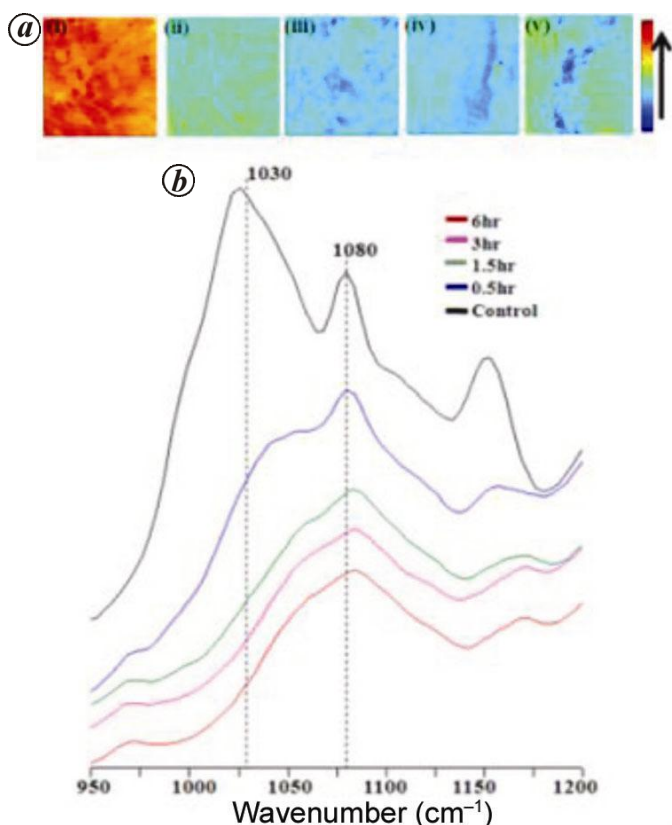


**Figure 9.** *a*, FTIR images of  $\sim 4 \mu\text{m}$  sections from control and APAP treated mice livers, colour coded at 1030  $\text{cm}^{-1}$ /1080  $\text{cm}^{-1}$  ratio which represents the glycogen distribution at different time points: (i) Control, (ii) 0.5 h, (iii) 1.5 h, (iv) 3 h and (v) 6 h – post APAP treatment, image area  $350 \times 350 \mu\text{m}^2$ . *b*, Corresponding FTIR spectra (950 to 1200  $\text{cm}^{-1}$ ) of control and APAP treated mice livers.

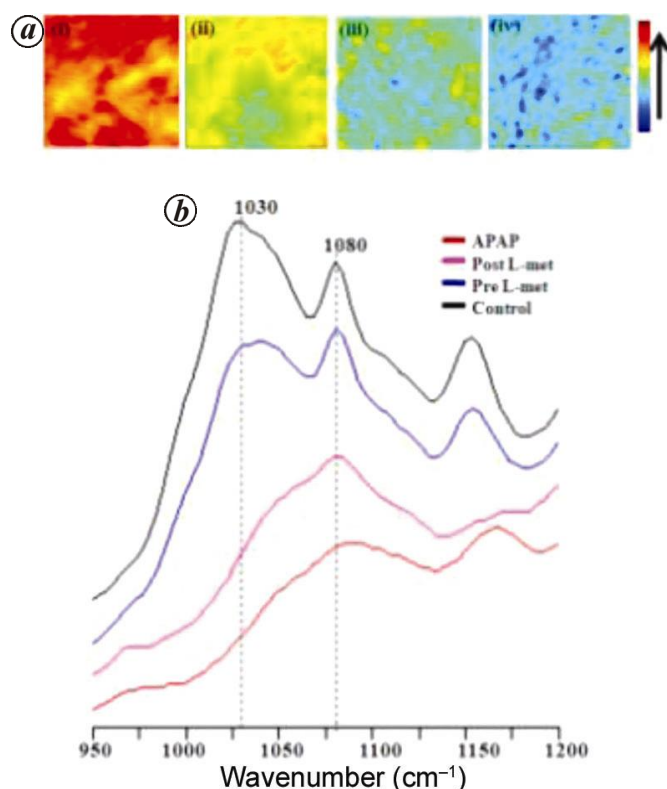


**Figure 10.** Effect of L-methionine treatment. *a*, FTIR images of  $\sim 4 \mu\text{m}$  sections from control and APAP-treated mice livers, colour coded at 1030  $\text{cm}^{-1}$ /1080  $\text{cm}^{-1}$  ratio which represents the glycogen distribution in the following order: (i) Control, (ii) Pre L-met, (iii) Post L-met and (iv) 6 h – post APAP treatment (without L-met), image area  $350 \times 350 \mu\text{m}^2$ . *b*, Corresponding FTIR spectra (950 to 1200  $\text{cm}^{-1}$ ) of control and treated mice livers.

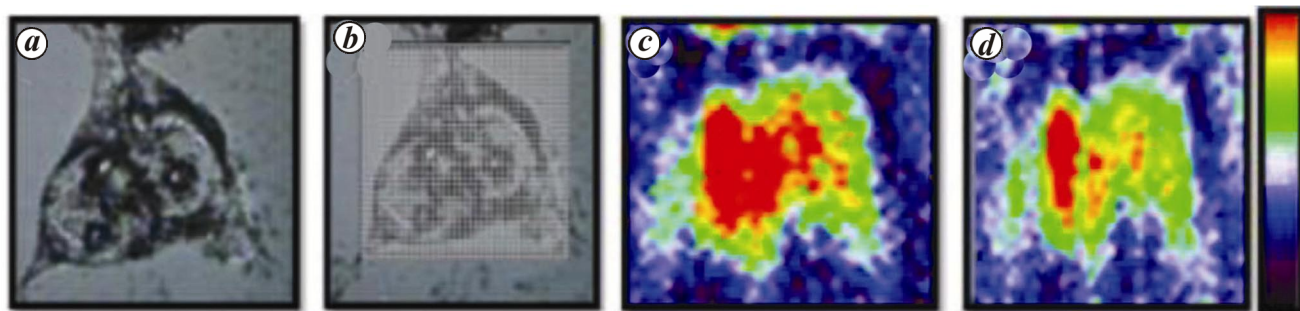


**Figure 11.** Raman imaging of breast cancer cell. *a*, White-light images of MCF7 cell; *b*, Selected area of cell for mapping (shown through grid); Raman images of whole single cells generated by (*c*) lipid peak ( $1447\text{ cm}^{-1}$ ) and (*d*) amide I peak ( $1662\text{ cm}^{-1}$ ).

of cell sorting and demonstrated that sampling of hESC-derived cardiomyocytes with a laser beam focused to a line could eliminate the need of cell raster scanning and achieve high prediction accuracies (>95% specificity and >96% sensitivity) with acquisition times  $\sim 5$  seconds per cell when the laser beam was focused to a  $\sim 2\text{ }\mu\text{m} \times 20\text{ }\mu\text{m}$  line. They have also monitored the cardiac differentiation of human embryonic stem cells *in vitro* by Raman spectroscopy<sup>50</sup>.

Currently, our group is working on breast cancer cell lines to understand the differences between aggressive and non-aggressive cells. We have recorded Raman image from fixed MCF7 cells, a breast cancer cell line, cultured on quartz substrates (Figure 11). Cells were cultured in Dulbecco's Modified Eagle's Medium (DMEM) (Sigma-Aldrich) supplemented with 10% Fetal Bovine Serum (FBS), penicillin (1 KU/ml) and streptomycin (0.1 mg/ml). The growth medium was aspirated from the sample prior to fixation and cells were washed several times with PBS. Then, the washed slides were dipped in methanol acetone mixture and were kept at  $-20^\circ\text{C}$  for 5 min. After that the slides were kept outside for drying at room temperature. Raman images were acquired by scanning the 785 nm diode line focus ( $\sim 28\text{ mW}$  at the sample) across a single cell with a piezoelectric stage. The excitation line was focused using a  $50\times$  L, NA = 0.50, long working distance objective and an integration time of 20 sec. The images are obtained at  $1662\text{ cm}^{-1}$  and at  $1447\text{ cm}^{-1}$ , depicting the distribution of protein and lipid respectively, across the cell.

### Multivariate analysis

Despite the above described sophisticated imaging techniques, there are several potential sources of artifacts and unwanted background in the acquired Raman and IR images, such as auto fluorescence of the samples, surface topography, i.e. unevenness, laser-induced photodegradation, cosmic rays and Mie scattering. Also, every pixel in the imaging data consists of as many as a thousand intensity points, each representing a different wavenumber, i.e.

a specific molecular vibration. Though adequate information can be obtained by following one of the vibrational bands, to use the full power of imaging very efficient modelling techniques employing multivariate analysis are required to extract the exact representation of the sample. These methods integrate the full spectral range available to handle huge imaging data sets. Some of those techniques are Principal Component Analysis (PCA), Linear Discriminant Analysis (LDA), Artificial Neural Nets (ANN), Principal Component Regression (PCR), Multiple Linear Regression (MLR), Cluster Analysis, and Partial Least Squares Regression (PLSR)<sup>51</sup>. In the literature multivariate analysis has been used widely in conjunction with Raman and FTIR imaging. Using multivariate analysis each point in a Raman or IR image can be automatically classified into various groups, according to the chemical components present in the sample. This automated grouping of the pixels having the same characteristic bands in an image is called clustering. This is done by considering two important criteria: (i) pixels in the same group are as similar as possible and (ii) pixels in different groups are as dissimilar as possible<sup>52-54</sup>. Milos *et al.* demonstrated that Raman imaging along with multivariate analysis has a distinct capacity for label-free detection of sub cellular components. They compared various multivariate methods such as K-means cluster analysis (KMCA), agglomerative hierarchical cluster analysis (AHCA), PCA, vertex component analysis (VCA) and divisive correlation cluster analysis (DCCA) and concluded that for cells and tissue sections, where the spectral contrast between components is subtle, AHCA generally gives the best clustering<sup>52</sup>. Also, van Manen *et al.*<sup>53</sup> have successfully applied Raman (label-free) imaging along with AHCA to analyse the chemical composition of sub cellular components such as lipid bodies. A PCA-LDA based model was also applied to label-free Raman images to discriminate between undifferentiated neural stem cells and glial cells<sup>54</sup>.

At present we are also trying to understand the composition and function of hippocampal neurons in a rat model using Raman imaging along with multivariate analysis.

Raman images were generated by raster-scanning the laser beam (785 nm) over the hippocampal neuron (Figure 12 *a*). The excitation line was focused using a 63 $\times$ , NA = 0.9, water immersion objective for an integration time of 5 sec using an inverted microscope system. In the present study, the neuron image is classified into two and four clusters, using AHCA to visualize regions with high Raman spectral similarities. As a significant part of the image represents only substrate and buffer (background), a high-SNR filter is employed to make sure such unwanted signals are removed prior to multivariate analysis (black regions in Figure 12 *b* and *c*). Subsequently, each spectrum in the image was baseline corrected, smoothed and normalized to eliminate effects of instrumental drift. In order to reduce dimensionality, eliminate noise and improve computational efficiency, PCA was performed prior to cluster analysis<sup>53</sup>. The 30 most significant principal component scores were retained as input for AHCA for clustering and the corresponding average spectra from each cluster were plotted (Figure 12 *d* and *e*). As shown in Figure 12, in case of two clusters the neuron was separated into nucleus (cyan) and cytoplasm (red), which could be differentiated by the intensity of the DNA bands at 782 cm<sup>-1</sup>. In case of four clusters, 'cyan' represents the segment where the thickness of sample is relatively low. Overall, we could divide the Raman image according to the chemical components and their relative intensity using multivariate analysis quite effectively.

### Recent advancements

Raman and MIR imaging techniques have very high multiplexing capabilities as the molecules can be differentiated by their spectral fingerprints<sup>55</sup>. However, the Raman effect is inherently weak, typically only one photon is inelastically scattered out of 10<sup>6</sup> elastically scattered photons; this limits the sensitivity and hence restricts the applications of Raman in various fields. On the other hand, MIR provides comparatively strong signals but is limited by a trade-off between spatial resolution, acquisition time and SNR. Also, water has a strong absorption in the mid-IR region, which limits the diagnostic capabilities of MIR spectroscopy for aqueous-based preparations. Many efforts have been made to overcome the constraints associated with the above-mentioned techniques.

Resonance Raman Spectroscopy (RRS), Surface-Enhanced Raman Spectroscopy (SERS), Surface-Enhanced Resonance Raman Spectroscopy (SERRS), Stimulated Raman Scattering (SRS) and Coherent Anti-Stokes Raman Scattering (CARS) are techniques used to enhance the weak Raman signals or to increase the signal to background ratio<sup>56-64</sup>. In RRS the excitation wavelength is in resonance with an electronic transition of the molecule, which leads to a major enhancement of those modes that are coupled to the electronic transitions<sup>56</sup>. However, the

fluorescence background may become a problem unless excitation in the UV range (<250 nm) is employed. In that case extra selectivity for UV-absorbing compounds is obtained (e.g. DNA bases, aromatic amino acids, nitro-toluene-type explosives), but instrumentation will be more expensive as all the microspectrometer components must be UV-transparent. Alternatively, SERS is observed when the analyte is adsorbed on a roughened metal surface or nanoparticles<sup>57</sup>. Usually, copper, silver or gold are being used for SERS studies as their plasmons have absorption in the visible or NIR region. However, in recent times single-walled carbon nanotubes (SWNTS) and quantum dots have also been extensively used for SERS studies<sup>58-60</sup>. The imaging of SERS active nanoparticles, SWNTS, quantum dots, etc. have significant potential as a real-time *in vivo* tissue diagnostic technique, as it is minimally invasive. Deep-tissue imaging in small animals using nanoparticles and SWNTS has also been done to demonstrate the applicability of Raman imaging, which has very high multiplexing capability, as a clinical diagnostic tool<sup>58</sup>.

The techniques discussed so far are relatively slow and therefore suitable only for the study of static systems. Much faster imaging is required for dynamic studies. In this context, nonlinear Raman imaging techniques have an edge over conventional Raman imaging. CARS is based on resonant excitation with three photons from at least two different pulsed lasers which enhances the Raman scattering and is free from the red shifted auto-fluorescence of the sample; consequently high quality images can be acquired in a few seconds<sup>61</sup>. However, it is limited to the excitation of only one vibrational frequency rather than a full spectrum. The use of one laser with a broad spectral range can circumvent this problem by exciting many vibrations at once, which is named 'Multiplex CARS'. CARS imaging has demonstrated the ability to probe the molecules in live cells, noninvasively and selectively<sup>62</sup>. CARS microscopy offers much higher sensitivity than spontaneous Raman microscopy (enabling much faster imaging), but the presence of non-resonant background complicates the interpretation of imaging data. On the other hand, SRS imaging, a technique that also requires two pulsed lasers, does not exhibit non-resonant background and offers readily interpretable chemical contrast. SRS offers a new label free mapping approach for studying the dynamics in living cells and organisms and even video-rate imaging has been demonstrated, although this can be achieved for only one vibrational band at a time and advanced instrumentation is required<sup>63-65</sup>.

Generally, the laser spot size determines the spatial resolution; confocal micro-Raman spectroscopy can achieve a spatial resolution of about 300 nm for visible light focus which is governed by the diffraction limit as discussed above<sup>66,67</sup>. Strong efforts have been made to improve the resolution further beyond the diffraction

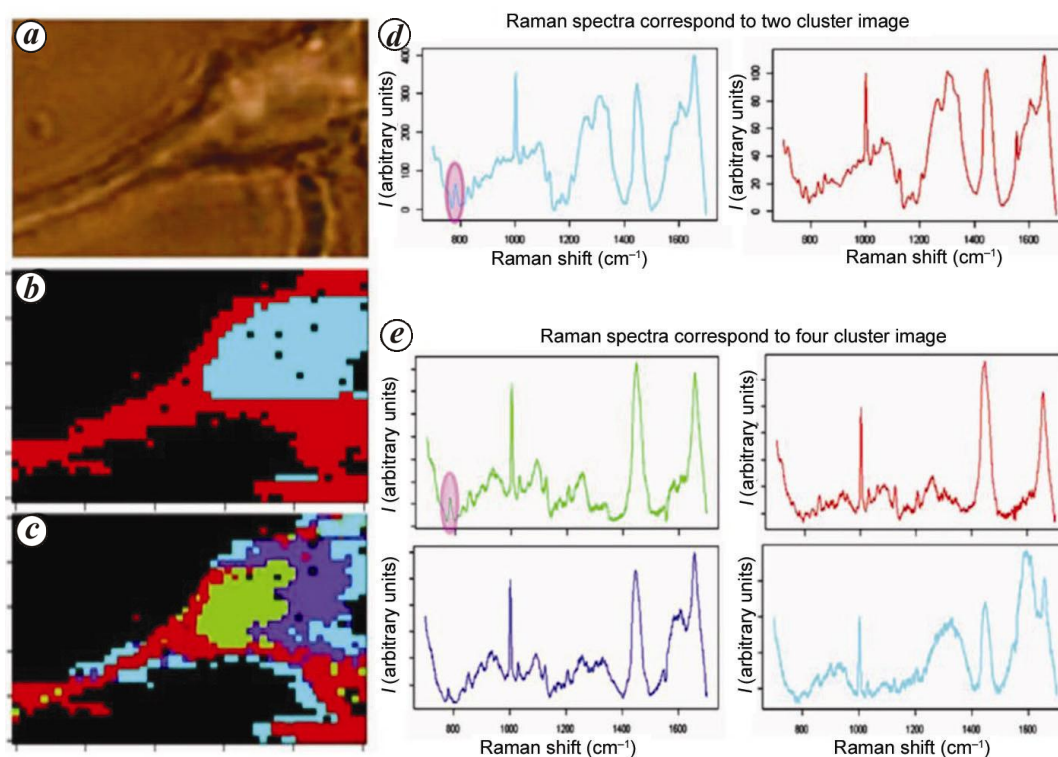


**Figure 12.** Multivariate analysis of Raman image of a neuron cell. *a*, White-light image; *b* and *c* are the corresponding Raman images of two and four clusters respectively, obtained using the AHCA multivariate technique; *d*, Average Raman spectra of two clusters; *e*, Average Raman spectra of four clusters. Black regions indicate low SNR signals that were removed during the preprocessing stage.

limit to extend the application of Raman spectroscopy towards the field of nanoscience and nanotechnology. Scanning Near-field Microscopy (SNOM) has been employed to overcome the diffraction limit in two different ways: (i) with an aperture and (ii) apertureless (tip-enhanced near-field techniques). In the former an optical fibre with a very small aperture (50–100 nm) is used to deliver the laser light to the sample or collect emitted photons from a small area. However, this method suffers from the very low throughput through such apertures and the inherent weakness of the Raman scattering. Alternatively, an apertureless technique, tip-enhanced Raman scattering (TERS), is used in which the tip apex creates a strongly confined optical field within the laser spot. TERS microscopy can provide a spatial resolution that is almost 35 times smaller than the wavelength of the probing light, i.e. in the range of few nanometers. The Raman signal is enhanced near the silver or gold tip due to resonant excitation of surface plasmon polaritons. Unlike SERS, TERS can not only provide enhancement but by scanning the metallic tip over the sample it can also construct Raman images with extremely high resolution<sup>66–68</sup>. In the case of mid-IR microscopy the spatial resolution is normally even poorer than conventional Raman microspectroscopy, due to the wavelength of the light used (2.5–25  $\mu\text{m}$ ). The recent integration of AFM, which

offers excellent spatial resolution, with IR spectroscopy enables the recording of IR spectra and images with a spatial resolution in the range of 50 to 100 nm, which is far better than conventional IR microspectroscopy<sup>69</sup>. The technique is based on local heating when the frequency of a tunable laser matches the IR absorption spectrum of a component close to the surface of the sample. The resulting expansion is registered by AFM. Raman and IR microscopy methods are confined to the surface or to the focal plane just below the surface ( $\sim 100 \mu\text{m}$  max). Depth Raman analysis has been reported using spatially offset Raman Spectroscopy (SORS) and universal multiple angle Raman spectroscopy (UMARS) but at greater depths one loses spatial resolution due to multiple scattering<sup>70,71</sup>.

The recent developments in background-free and highly efficient optical fibres have opened possibilities to use Raman and IR imaging for probing deeper tissues in the field of medicine. Raman imaging techniques using optical fibres lead to endoscopic applications which would be useful for *in vivo* diagnosis in real time<sup>72,73</sup>. Raman spectra of brain tissues of live mice and rats have been successfully obtained using a ball lens hollow fibre Raman probe using a background-free electronically tuned Ti:sapphire laser in the fingerprint region and in the high-wavenumber region from the same measurement

point at the same time<sup>72</sup>. Okagbare *et al.*<sup>73</sup> have also employed Raman spectroscopy for *in vivo* assessment of allograft implantation in a rat model. They could successfully record Raman spectra from the bone mineral matrix and demonstrated a proof-of-concept that fibre-optic Raman probes can be used to monitor bone quality non-invasively. In the case of IR, the fibre optics are used with an ATR probe (Ge, diamond, etc.) which allows non-destructive measurements *in vivo* as ATR is a surface technique. In addition, it has advantages over conventional MIR microscopy methods as it requires no sample preparation and can probe an area at the centimetre level, thus reflecting the true comprehensive information of the malignant tissues<sup>74,75</sup>. Furthermore, the achievable spatial resolution, which is restricted by the refractive index of the material between the sample and the collecting objective lens, gets better with the ATR-IR fibre-optic technique. Also, the effective optical path length is very small because the evanescent wave extends only up to 0.5–2  $\mu\text{m}$  beyond the crystal. This allows the analysis of highly absorbing samples or samples in aqueous environments. The application of MIR microspectroscopy in biological research could be substantially increased if spectral imaging at high spatial resolution becomes possible in order to reveal domains or structures at the cellular or sub-cellular scale in short time frames. This can be achieved using powerful IR sources, such as multiple synchrotron beams, in combination with focal plane array detectors which considerably increases the SNR and hence reduces the collection time<sup>76,77</sup>. Synchrotron radiation-based IR microspectroscopy has been employed for the characterization of single cells but it has been almost exclusively limited to fixed or dried cells to avoid background from aqueous media which can be overcome with the help of an ATR system. Therefore, the combination of synchrotron beams with an ATR probe is the preferable option for MIR imaging in aqueous media.

## Summary

We have discussed different imaging methodologies, historical developments, technological advancements and specific applications of Raman and MIR imaging. Multiplexing advantage of the technique has been clarified in selected examples; from a simple two-component polymer-blend to multiple component explosives and to structurally more complex biological samples. To retrieve meaningful molecular information from a composite spectral data multivariate analytical techniques are often employed and are also briefly discussed. Raman microscopy has potential to fulfill the specific requirements in clinical biology. Vibrational imaging continues to advance by integrating with other imaging techniques and would benefit nano-technology and biomedicine in addressing several critical issues.

1. Keren, S., Zavaleta, C., Cheng, Z., de la Zerda, A., Gheysens, O. and Gambhir, S. S., Noninvasive molecular imaging of small living subjects using Raman spectroscopy. *PNAS*, 2008, **105**, 5844–5849.
2. Weissleder, R. and Pittet, M. J., Imaging in the era of molecular oncology. *Nature*, 2008, **452**, 580–589.
3. Otto, C., de Grauw, C. J., Duindam, J. J., Sijtsema, N. M. and Grev, J., Applications of micro-Raman imaging in biomedical research. *J. Raman Spectrosc.*, 1997, **28**, 143–150.
4. Chiu, L. D., Ando, M. and Hamaguchi, H., Study of the ‘Raman spectroscopic signature of life’ in mitochondria isolated from budding yeast. *J. Raman Spectrosc.*, 2010, **41**, 2–3.
5. Treado, P. J. and Morris, M. D., Infrared and Raman spectroscopic imaging. *Appl. Spectrosc. Rev.*, 1994, **29**, 1–38.
6. Delhaye, M. and Migeon, M., *Compt. Rend. Acad. Sci. Paris*, 1966, **262**, 702, 1513.
7. Delhaye, M. and Dhamelincourt, P., IVth International Conference on Raman Spectroscopy, Brunswick, ME, USA, 1974.
8. Rosasco, G. J., Etz, E. S. and Cassatt, W. A., IVth International Conference on Raman Spectroscopy, Brunswick, ME, USA, 1974.
9. Everall, N., Depth profiling with confocal Raman microscopy, Part I. *Spectroscopy*, 2004, **19**, 22–27.
10. Christoph, K., Bioanalytical applications of Raman spectroscopy, *Anal. Bioanal. Chem.*, 2004, **378**, 60–62.
11. Sijtsema, N. M., Wouters, S. D., De Grauw, C. J., Otto, C. and Greve, J., Confocal direct imaging Raman microscope: design and applications in biology. *Appl. Spectrosc.*, 1998, **52**(3), 348–355.
12. Delhaye, M. and Dhamelincourt, P., Raman microprobe and microscope with laser excitation. *J. Raman Spectrosc.*, 1975, **3**, 33–43.
13. Barbillat, J., Dhamelincourt, P., Delhaye, M. and Dilor, E. Da, S., Raman confocal microprobing, imaging and fibre-optic remote sensing: a further step in molecular analysis. *J. Raman Spectrosc.*, 1994, **25**, 3–11.
14. Schlucker, S., Schaeberle, M. D., Huffman, S. W. and Levin, I. W., Raman microspectroscopy: a comparison of point, line and wide-field imaging methodologies. *Anal. Chem.*, 2003, **75**, 4312–4318.
15. Ivanda, M. and Furic, K., Line focusing in micro-Raman spectroscopy. *Appl. Opt.*, 1992, **31**, 6371–6375.
16. Puppels, G. J., Grond, M. and Greve, J., Direct imaging Raman microscope based on tunable wavelength excitation and narrow-band emission detection. *Appl. Spectrosc.*, 1993, **47**, 1255–1267.
17. Ling, J., Weitman, S. D., Miller, M. A., Moore, R. V. and Bovik, A. C., Direct Raman imaging techniques for study of the subcellular distribution of a drug. *Appl. Opt.*, 2002, **41**, 6006–6017.
18. Markwort, L., Kip, B., Da Silva, E. and Roussel, B., Raman imaging of heterogeneous polymers: a comparison of global versus point illumination. *Appl. Spectrosc.*, 1995, **49**, 1411–1430.
19. Derrick, M. R., Stulik, D. and Landry, J. M., *Infrared spectroscopy in conservation science*, 1999 by the J. Paul Getty Trust.
20. Bhargava, R. and Levin, I. W., *Spectrochemical Analysis using Infrared Multichannel Detectors*, Blackwell Publishing Ltd, 2005.
21. Lasch, P. and Naumann, D., Spatial resolution in infrared microspectroscopic imaging of tissues. *Biochim. Biophys. Acta*, 2006, **1758**, 814–829.
22. Han, C. C. and Akcasu, A. Z., Phase decomposition in polymers. *Annu. Rev. Phys. Chem.*, 1992, **43**, 61–90.
23. de León, A. S., Campo, A., García, M. F., Hernández, J. R. and Bonilla, A. M., Hierarchically structured multifunctional porous interfaces through water templated self-assembly of ternary systems. *Langmuir*, 2012, **28**, 9778–9787.
24. Stevenson, R., Arias, A. C., Ramsdale, C., MacKenzie, J. D. and Richards, D., Raman microscopy determination of phase composition in polyfluorene composites. *Appl. Phys. Lett.*, 2001, **79**, 2178–2180.

25. Padilla, A. M., Ivanisevic, I., Yang, Y., Engers, D., Bogner, R. H. and Pikal, M. J., The study of phase separation in amorphous freeze-dried systems. Part I: Raman mapping and computational analysis of XRPD data in model polymer systems. *J. Pharm. Sci.*, 2011, **100**, 206–222.
26. Breitzkreitz, M. C. and Poppi, R., Trend in Raman chemical imaging. *J. Biomed. Spectrosc. Imaging*, 2012, **1**, 159–183.
27. Zhou, D., Shi, A. C. and Zhang, P., Numerical simulation of phase separation coupled with crystallization. *J. Chem. Phys.*, 2008, **129**, 15490:1–8.
28. Samuel, A. Z. and Umaphathy, S., Energy funneling and macromolecular conformational dynamics: a 2D Raman correlation study of PEG melting. *Polym. J. (Nature)*, 2014, **46**, 330–336.
29. Samuel, A. Z., Umaphathy, S. and Ramakrishnan, S., Functionalized and postfunctionalizable porous polymeric films through evaporation-induced phase separation using mixed solvents. *ACS Appl. Mater. Interfaces*, 2011, **3**, 3293–3299.
30. Sil, S., Kuhar, N., Acharya, S. and Umaphathy, S., Is chemically synthesized graphene ‘really’ a unique substrate for SERS and fluorescence quenching? *Sci. Rep.*, 2013, **3**, 3336, 1–6.
31. Ni, Z., Wang, Y., Yu, T. and Shen, Z., Raman spectroscopy and imaging of graphene. *Nano Res.*, 2008, **1**, 273–291.
32. Emmons, E. D., Tripathi, A., Guicheteau, J. A., Christesen, S. D. and Fountain, A. W., Raman chemical imaging of explosive-contaminated fingerprints. *Appl. Spectrosc.*, 2009, **63**, 1197–1203.
33. Ali, E. M. A., Edwards, H. G. M., Hargreaves, M. D. and Scowen, I. J., Detection of explosives on human nail using confocal Raman microscopy. *J. Raman Spectrosc.*, 2009, **40**, 144–149.
34. Widjaja, E., Lee, W. L. and Joachim Loo, S. C., Application of Raman microscopy to biodegradable double-walled microspheres. *Anal. Chem.*, 2010, **82**, 1277–1282.
35. Bratashov, D. N. *et al.*, Raman imaging and photodegradation study of phthalocyanine containing microcapsules and coated particles. *J. Raman Spectrosc.*, 2011, **42**, 1901–1907.
36. Rafferty, D. W. and Koenig, J. K., FTIR imaging for the characterization of controlled-release drug delivery applications. *J. Controlled Release*, 2002, **83**, 29–39.
37. Draux, F., Gobinet, C., Sule-Suso, J., Manfait, M., Jeannesson, P. and Sockalingum, G. D., Raman imaging of single living cells: probing effects of non-cytotoxic doses of an anti-cancer drug. *Analyst*, 2011, **136**, 2718–2725.
38. Harrigan, G. *et al.*, Application of high-throughput Fourier-transform infrared spectroscopy in toxicology studies: contribution to a study on the development of an animal model for idiosyncratic toxicity. *Toxicol. Lett.*, 2004, **146**, 197–205.
39. Gautam, R., Chandrasekar, B., Deobagkar-Lele, M., Rakshit, S., Kumar, B. N. V., Nandi, D. and Umaphathy, S., Identification of early biomarkers during acetaminophen-induced hepatotoxicity by Fourier transform infrared microspectroscopy. *PLoS ONE*, 2012, **7**(9): e45521.
40. Kalasinsky, K. S. *et al.*, Raman chemical imaging spectroscopy reagentless detection and identification of pathogens: signature development and evaluation. *Anal. Chem.*, 2007, **79**, 2658–2673.
41. Walter, A., Schumacher, W., Bocklitz, T., Reinicke, M., Rosch, P., Kothe, E. and Popp, J., From bulk to single-cell classification of the filamentous growing streptomyces bacteria by means of Raman spectroscopy. *Appl. Spectrosc.*, 2011, **65**, 1116–1125.
42. Davis, R. and Mauer, L. J., Fourier transform infrared (FTIR) spectroscopy: a rapid tool for detection and analysis of foodborne pathogenic bacteria. *Curr. Res. Technol. Educ. Topics Appl. Microbiol. Biotechnol.*, 2010, **2**, 1582–1594.
43. Petrich, W., Mid-infrared and Raman spectroscopy for medical diagnostics. *Appl. Spectrosc. Rev.*, 2001, **36**, 181–237.
44. Singh, B. *et al.*, Application of vibrational microspectroscopy to biology and medicine. *Curr. Sci.*, 2012, **102**, 232–244.
45. Saxena, T., Deng, B., Stelzner, D., Hasenwinkel, J. and Chaiken, J., Raman spectroscopic investigation of spinal cord injury in a rat model. *J. Biomed. Opt.*, 2011, **16**, 027003-1-14.
46. Pezolet, M. and Georgescaul, D., Raman spectroscopy of nerve fibers a study of membrane lipids under steady state conditions. *Biophys. J.*, 1985, **47**, 367–372.
47. Downes, A., Mouras, R. and Elfick, A., Optical spectroscopy for noninvasive monitoring of stem cell differentiation. *J. Biomed. Biotechnol.*, 2010, **101864**, 1–10.
48. Ami, D. *et al.*, Embryonic stem cell differentiation studied by FT-IR spectroscopy. *Biochim. Biophys. Acta*, 2008, **1783**, 98–106.
49. Pascut, F. C., Goh, H. T., George, V., Denning, C. and Nottingher, I., Toward label-free Raman-activated cell sorting of cardiomyocytes derived from human embryonic stem cells. *J. Biomed. Opt.*, 2011, **16**(4), 045002.
50. Pascut, F. C., Kalra, S., George, V., Welch, N., Denning, C. and Nottingher, I., Non-invasive label-free monitoring the cardiac differentiation of human embryonic stem cells in-vitro by Raman spectroscopy. *Biochim. Biophys. Acta*, 2013, **1830**, 3517–3524.
51. Mutha, L. and Mutha, R., Mining in chemometrics. *Anal. Chim. Acta*, 2008, **612**, 1–18.
52. Miljkovic, M., Chernenko, T., Romeo, M. J., Bird, B., Matthäus, C. and Diem, M., Label-free imaging of human cells: algorithms for image reconstruction of Raman hyperspectral datasets. *Analyst*, 2010, **135**, 2002–2013.
53. Van Manen, H. J., Kraan, Y. M., Roos, D. and Otto, C., Single-cell Raman and fluorescence microscopy reveal the association of lipid bodies with phagosomes in leukocytes. *PNAS*, 2005, **102**(29), 10159–10164.
54. Ghita, A. and Pascut, F. C., Cytoplasmic RNA in undifferentiated neural stem cells: a potential label-free Raman spectral marker for assessing the undifferentiated status. *Anal. Chem.*, 2012 **3**, **84**(7), 3155–3162.
55. Diem, M., Mazur, A., Lenau, K., Schubert, J., Bird, B., Miljković, M., Krafft, C. and Popp, J., Molecular pathology via IR and Raman spectral imaging. *J. Biophotonics*, 2013, **6**, 855–886.
56. Asher, S. A., UV resonance Raman spectroscopy for analytical, physical and biophysical chemistry. *Anal. Chem.*, 1993, **65**(2), 59A–66A.
57. Fleischmann, M., Hendra, P. J. and McQuillan, A., Raman spectra of pyridine adsorbed at a silver electrode. *J. Chem. Phys. Lett.*, 1974, **26**, 163–166.
58. Keren, S., Zavaleta, C., Cheng, Z., de la Zerda, A., Gheysens, O. and Gambhir, S. S., Noninvasive molecular imaging of small living subjects using Raman spectroscopy. *PNAS*, 2008, **105**(15), 5844–5849.
59. Milekhin, A. G., Sveshnikova, L. L., Duda, T. A., Surovtsev, N. V., Adichtchev, S. V. and Zahn, D. R. T., Surface enhanced Raman scattering by CdS quantum dots. *JETP Lett.*, 2008, **88**(12), 799–801.
60. Michalet, X. *et al.*, Quantum dots for live cells, *in vivo* imaging and diagnostics. *Science*, 2005, **307**, 538–544.
61. Rodriguez, L. G., Lockett, S. J. and Holtom, G. R., Coherent anti-stokes Raman scattering microscopy: a biological review. *Cytometry Part A*, 2006, **69**, 779–791.
62. Downes, A., Mouras, R., Bagnaninchi, P. and Elfick, A., Raman spectroscopy and CARS microscopy of stem cells and their derivatives. *J. Raman Spectrosc.*, 2011, **42**, 1864–1870.
63. Freudiger, C. W. *et al.*, Label-free biomedical imaging with high sensitivity by stimulated Raman scattering microscopy. *Science*, 2008, **322**, 1857–1861.
64. Saar, B. G., Freudiger, C. W., Reichman, J., Stanley, C. M., Holtom, G. R. and Xie, X. S., Video-rate molecular imaging *in vivo* with stimulated Raman scattering. *Science*, 2010, **330**, 1368–1370.
65. Fu, D., Lu, F. K., Zhang, X., Freudiger, C. W., Pernik, D. R. Holtom, G. R. and Xie, X. S., Quantitative chemical imaging with

- multiplex stimulated Raman scattering microscopy. *J. Am. Chem. Soc.*, 2012, **134**, 3623–3626.
66. Kasim, J., Ting, J. Y., Meng, Y. Y., Ping, L. J., See, A., Jong, L. L. and Xiang, S. Z., Near-field Raman imaging using optically trapped dielectric microsphere. *Optics Express*, 2008, **16**, 7976–7984.
67. Verma, P., Ichimura, T., Yano, T. A., Saito, Y. and Kawata, S., Nano-imaging through tip-enhanced Raman spectroscopy: stepping beyond the classical limits. *Laser Photon. Rev.*, 2010, **4**, 548–561.
68. Kurouski, D., Postiglione, T., Deckert-Gaudig, T., Deckert, V. and Lednev, I. K., Amide I vibrational mode suppression in surface (SERS) and tip (TERS) enhanced Raman spectra of protein specimens. *Analyst*, 2013, **138**, 1665–1673.
69. Dazzi, A., Prater, C. B., Hu, Q., Chase, D. B., Rabolt, J. F. and Marcott, C., AFM-IR: combining atomic force microscopy and infrared spectroscopy for nanoscale chemical characterization. *Appl. Spectrosc.*, 2012, **66**, 1365–1384.
70. Matousek, P. *et al.*, Subsurface probing in diffusely scattering media using spatially offset Raman spectroscopy. *Appl. Spectrosc.*, 2005, **59**, 393–400.
71. Sil, S. and Umapathy, S., Raman spectroscopy explores molecular structural signatures of hidden materials in depth: universal multiple angle Raman spectroscopy. *Sci. Rep.*, **4**, 5308-1-7.
72. Sato, H., Yamamoto, Y. S., Maruyama, A., Katagiri, T., Matsuura, Y. and Ozaki, Y., Raman study of brain functions in live mice and rats: a pilot study. *Vibr. Spectrosc.*, 2009, **50**, 125–130.
73. Okagbare, P. I., Esmonde-White, F. W. L., Goldstein, S. A. and Morris, M. D., Development of non-invasive Raman spectroscopy for *in vivo* evaluation of bone graft osseointegration in a rat model. *Analyst*, 2010, **135**, 3142–3146.
74. Wu, J. G. *et al.*, Distinguishing malignant from normal oral tissues using FTIR fiber-optic techniques. *Biopolymers (Biospectroscopy)*, 2001, **62**, 185–192.
75. McFearin, C. L., Sankaranarayanan, J. and Almutairi, A., Application of fiber-optic attenuated total reflection-FT-IR methods for *in situ* characterization of protein delivery systems in real time. *Anal. Chem.*, 2011, **83**, 3943–3949.
76. Vaccari, L., Birarda, G., Grenzi, G., Pacor, S. and Businaro, L., Synchrotron radiation infrared microspectroscopy of single living cells in microfluidic devices: advantages, disadvantages and future perspectives. *J. Phys.: Conf. Ser.*, 2012, **359**, 012007:1-10.
77. Nasse, M. J. *et al.*, High-resolution Fourier-transform infrared chemical imaging with multiple synchrotron beams. *Nature Methods*, 2011, **8**, 413–418.

**ACKNOWLEDGEMENTS.** The authors gratefully acknowledge Prof. D. Nandi (BC, IISc), Prof. S. Ramakrishnan (IPC, IISc), Dr A. Ranganathan (MRDG, IISc) and Prof. S. K. Sikdar (MBU, IISc) for providing samples and Sandeep Vanga for his help with the cluster analysis. We also would like to thank the Indian Institute of Science, Council of Scientific and Industrial Research, Department of Biotechnology and Department of Science and Technology, Government of India, for the financial support. SU acknowledges the J.C. Bose fellowship from DST.

**Competing interests.** The authors declare that they have no competing interests.

Received 4 November 2014; accepted 25 December 2014